ELSEVIER

Chemical Engineering Journal 137 (2008) 411–421

Chemical Engineering Journal

www.elsevier.com/locate/cej

Evaluation of high-emissivity coatings in steam cracking furnaces using a non-grey gas radiation model

G.D. Stefanidis, K.M. Van Geem, G.J. Heynderickx *, G.B. Marin

Laboratorium voor Petrochemische Techniek (LPT), Ghent University, Krijgslaan 281 Block S5, Ghent B9000, Belgium

Received 3 November 2006; received in revised form 27 April 2007; accepted 28 April 2007

Abstract

The efficiency of the application of high-emissivity coatings on the furnace walls in steam cracking technology can only be evaluated on the basis of a description of radiative heat transfer distinguishing between the frequency bands. To this end, a non-grey gas radiation model based on the exponential wide band model (EWBM) has been developed and applied in the context of three-dimensional CFD simulations of an industrial naphtha cracking furnace with side-wall radiation burners. Applying a high-emissivity coating on the furnace wall decreases the net outgoing radiation from the furnace wall in the absorption bands and increases the net outgoing radiation from the furnace wall in the clear windows. Since radiation that is emitted by the furnace wall and travels through the flue gas in the clear windows can reach the reactor tubes without partially being absorbed by the flue gas, contrary to radiation that is emitted by the furnace wall and travels through the flue gas in the absorption bands, the thermal efficiency of the furnace increases. It was found that application of a high-emissivity coating on the furnace walls improves the thermal efficiency of the furnace (∼1%), the naphtha conversion (∼1%) and the ethylene yield (∼0.5%). These differences are small but, considering the industrial importance and scale of the steam cracking process, significant.

Keywords: Steam cracking furnaces; High-emissivity coatings; Radiation; Non-grey gas model

1. Introduction

Steam cracking of hydrocarbons to olefins is an endothermic process carried out in tubular reactor coils suspended in large gas fired furnaces. Due to the high temperature of the combustion gases and the furnace walls, radiation is the predominant mode of heat transfer in the furnace. Considering the scale and the importance of the industrial process even a small rise in thermal efficiency (fraction of the furnace energy input absorbed by the reactor coils) can be translated into an important increase in the olefin yields or an important decrease in the required fuel gas input. The application of ceramic high-emissivity coatings on the internal surface of furnace walls is believed to result in an increase in thermal efficiency [1]. In general, a high-emissivity ceramic coating for refractory linings maximizes and stabilizes the emissivity over varying process temperatures, thus promoting rapid and efficient heat transfer, uniform heating and extended refractory life. The emissivity of most refractory materials (alumina- and silica-based materials), which are used for high-temperature industrial applications (heaters, furnaces, kilns, ovens in iron and steel industry, glass industry, cement industry, refineries, petrochemical industry, etc.), such as firebrick, insulating firebrick, high alumina brick and ceramic fibre decreases with temperature. On the contrary, the emissivity of a high-emissivity ceramic coating increases with temperature.

The effect of high-emissivity furnace wall coatings on the furnace thermal efficiency is explained on the basis of the fundamental difference between radiation in gases and radiation from surfaces. Surfaces absorb and emit radiation at all frequencies. Gases absorb and emit radiation at certain discrete frequencies. Due to various overlapping effects, these absorption lines form absorption bands. Spectral intervals in which no radiation is absorbed or emitted, the so-called clear windows, are positioned in between the absorption bands. Firstly, the application of a high-emissivity coating on a furnace wall implies that the amount of radiation energy that is reflected by the wall decreases. Second, the amount of radiation energy that is absorbed by the wall increases. As the furnace walls are insulated and the heat losses to the environment are small, more of this energy

* Corresponding author. Tel.: +32 9 264 4516; fax: +32 9 264 4999.
E-mail address: geraldine.heynderickx@UGent.be (G.J. Heynderickx).

1385-8947/$ – see front matter © 2007 Elsevier B.V. All rights reserved.
doi:10.1016/j.cej.2007.04.042

Nomenclature

A	band absorption or "effective bandwidth" (m^{-1})
A^*	dimensionless band absorption
b	self-broadening to foreign-gas broadening ratio
$c_{p,j}$	heat capacity of component j (kJ/(kmol K))
$C_{1\varepsilon}$, $C_{2\varepsilon}$, $C_{3\varepsilon}$	model constants in the standard k–ε model
d_t	internal tube diameter (m)
E	total energy (m^2/s^2)
f	fanning friction factor
$f(T/\nu)$	fraction of the black body emissive power
F_j	molar flow rate (kmol/s)
$\vec{g}$	gravitational acceleration (m/s^2)
G_b	generation of turbulent kinetic energy due to buoyancy (W/m^3)
G_k	generation of turbulent kinetic energy due to mean velocity gradients (W/m^3)
h	specific enthalpy (J/kg)
$-\Delta H_k$	Heat of reaction k (kJ/kmol)
I	radiation intensity ($J/(m^2\ s)$)
$\vec{J}$	diffusion flux (kg/m^2)
k	production rate of turbulent kinetic energy (m^2/s^2)
k	molecular conductivity (W/(m K))
k_t	turbulent conductivity (W/(m K))
k_{eff}	effective conductivity ($k + k_t$) (W/(m K))
L	mean beam length (m)
n	empirical factor
n	refractive index
$\vec{n}$	normal pointing out of the domain
n_{kj}	stoichiometric coefficient of the component j in reaction k
n_R	number of reactions
N	number of bands
N_r	number of reactions
P, p	pressure (Pa)
P_a	absorber partial pressure (Pa)
P_e	equivalent broadening pressure parameter
P_0	reference partial pressure, 101,325 Pa
q	heat flux (W/m^2, kW/m^2)
q_{rad}	volumetric heat release due to radiation (W/m^3)
$\vec{r}$	position vector
r_b	radius of the bend (m)
r_k	rate of reaction k
$\vec{s}$	direction vector
$\vec{s}'$	scattering direction vector
t	time (s)
T	temperature (K)
u	velocity of the process gas (m/s)
x	absorber mole fraction, $x = P_a/P$
X	density path length (kg/m^2)
z	axial coordinate (m)

Greek letters

α	integrated band intensity (m/kg)
α	unit conversion factor depending on the units of p
β	mean line width to spacing parameter
Δ	difference operator
ε	emissivity
ε	dissipation rate of turbulent kinetic energy (m^2/s^3)
Φ	phase function
η	the quantity βP_e
κ	absorption coefficient (m^{-1})
λ	wavelength (m)
μ	molecular viscosity (kg/(m s))
ν	wavenumber (m^{-1})
ρ	gas density (kg/m^3)
σ	Stefan–Boltzmann constant, $\sigma = 5.67 \times 10^{-8}$ J/s/(m^2 K^4)
σ_s	scattering coefficient (m^{-1})
σ_k, σ_ε	model constants in the standard k–ε model
τ	transmittance
$\bar{\bar{\tau}}$	stress tensor (N/m^2)
τ_H	maximum optical depth at the band head
$\vec{\upsilon}$	overall velocity vector (m/s)
ω	exponential decay width (m^{-1})
ω	circumference of the tube (m)
Ω	hemispherical solid angle (sr)
Ω'	solid angle (sr)
Ω'	cross-section (m^2)
ζ	Nekrasov factor for bends

Subscripts

b	black body
c	center
eff	effective (summation of molecular and turbulent properties)
in	incident
j	gaseous species
k	gas band
k	reaction
l	lower
min	minimum
max	maximum
out	outgoing
t	turbulent
u	upper
w	wall
z	band
λ	spectral

is re-radiated back in the furnace. Unlike the reflected energy that preserves its spectral character, the re-radiated energy is redistributed over the entire wavelength spectrum. As a consequence only part of the absorbed radiation is re-radiated within the range of absorption bands of the gas; the remaining part is re-radiated in clear windows [2]. Thus, in the event of a coated furnace, an additional amount of radiation passes via the clear windows to the reactor tubes without being absorbed by the gas medium. In this paper this theoretical approach is investigated

and confirmed by quantifying the relevant radiation fluxes on the furnace walls, on the reactor tubes and in the flue gas. Two coupled furnace/reactor simulations are performed in which different furnace wall emissivities are applied. The furnace calculations are based on the computational fluid dynamic (CFD) approach using commercial software (FLUENT) [3]. In order to assess the high-emissivity coating effectiveness a non-grey (banded) gas radiation model is needed. To this end, an adapted version of the exponential wide band model (EWBM) of Edwards [4] is developed and programmed as a stand-alone code, which is plugged into the CFD solver as a user-defined function (UDF). The reactor calculations are based on a plug flow reactor model in combination with a detailed reaction network for steam cracking of hydrocarbons. Information on the modeling and numerical procedures as well as the furnace geometry and operating conditions are given in the next sections.

2. Exponential wide-band model (EWBM)

2.1. Calculation of band transmittance

The EWBM provides a mathematical model to correlate experimental data and predict wide band properties. The model is based on the assumption that the rotation lines in the band are equally spaced and can be reordered in frequency to form an array with exponentially decreasing line intensities starting from the band center. Three parameters are required to specify the radiative properties. These are the integrated band intensity α, the exponential decay bandwidth ω, and the mean line width to spacing (a "line overlap") parameter β. Expressions and correlations for the functional dependence of α, β and ω have been developed in Edwards [4] and Edwards and Balakrishnan [5] and are not presented here.

Originally, Edwards [4] deduced correlations from a body of experimental data for the calculation of the band transmittance. The set of correlations consists of relations of linear, square root and logarithmic form with respect to the optical depth at the band head depending on the level of absorption strength of the band. The so-called four-region expression is given below:

$$A^* = \tau_H \quad \text{for } \tau_H \le 1 \le \eta \text{ or } \tau_H \le \eta \le 1 \text{ (linear regime)} \tag{1}$$

$$A^* = (4\eta\tau_H)^{1/2} - \eta \quad \text{for } \eta \le \tau_H \le 1/\eta \text{ with } \eta \le 1 \text{ (square root regime)} \tag{2}$$

$$A^* = \ln(\tau_H\eta)^{1/2} + 2 - \eta \quad \text{for } \frac{1}{\eta} \le \tau_H \le \infty \text{ with } \eta \le 1 \text{ (logarithmic regime)} \tag{3}$$

$$A^* = \ln\tau_H + 1 \quad \text{for } \tau_H \ge 1 \text{ and } \eta \le 1 \text{ (logarithmic regime)} \tag{4}$$

where $A^* = A/\omega$ is the dimensionless band absorption, $\tau_H = \alpha X/\omega$ is the maximum optical depth at the band head and $\eta = \beta P_e$. P_e is the equivalent broadening pressure parameter calculated as [4]:

$$P_e = \left\{ \left[\frac{P}{P_0} \right] [1 + (b-1)x] \right\}^n \tag{5}$$

The band absorption or "effective" bandwidth A can be interpreted as the width of a black band (i.e. completely absorbing band) centered about the middle of the real absorption band and absorbing the same amount of (radiative) energy as the real band. The band transmittance is calculated from

$$\tau = \frac{\tau_H}{A^*} \frac{dA^*}{d\tau_H} \tag{6}$$

and the bandwidth from

$$\Delta\nu = \frac{A}{1-\tau} \tag{7}$$

Use of Eq. (6) implies a grey gas assumption for each band that breaks down at small path lengths. For that reason Edwards [4] suggested an upper limit for the calculation of the band transmittance:

$$\tau = \min(\tau, 0.9) \tag{8}$$

Imposing an upper limit for the band transmittance may introduce serious mistakes if a recursive relationship is used due to the strong dependence on the grid resolution [6]. One way to mitigate the problem is to define the band limits from the average properties of the domain in a preprocessing step. Then the band transmittance can be calculated from the following equation:

$$\tau = 1 - \frac{A}{\Delta\nu_{fix}} \tag{9}$$

Using the latter approach, the band absorption A is still calculated from the four-region expression (Eqs. (1)–(4)) and the temperature and composition dependence are still taken into account. However, instead of calculating the band transmittance using Eq. (6) in a first step, the bandwidth $\Delta\nu_{fix}$ is computed from the average properties of the domain as a first step.

2.2. Non-grey gas modeling

Four absorption bands are considered in this work. In these bands, carbon dioxide and water vapor are regarded as the only components of the combustion gases that absorb and emit radiation. These bands are referred to as

- CO_2: 15 μm, 4.3 μm, 2.7 μm.
- H_2O: 6.3 μm, 2.7 μm.

Distinct absorption coefficients are derived for the distinct absorption bands. In brief, the band transmittance (Eq. (6)) and the bandwidth (Eq. (7)) are first calculated over the range 1000–1900 K using the four-region expression. Next, an average width for each band is computed and remains fixed for the recalculation of the band transmittances over the range 1000–1900 K using Eq. (9). It is noted here that the computed bandwidths do not change considerably with temperature and thus a simple arithmetic average bandwidth is considered representative

for each band. In this approach an arbitrary upper limit for the band transmittance, as explained in Section 2.1, is not imposed. The fixed bandwidth is also used for the computation of fixed band limits over which the radiative transfer equation (RTE) is solved. In case of a symmetric band k where the band center $\nu_{c,k}$ is specified, the upper and the lower limits are

$$\nu_{u,k} = \nu_{c,k} + \frac{\Delta\nu_k}{2} \quad \text{and} \quad \nu_{l,k} = \nu_{c,k} - \frac{\Delta\nu_k}{2} \tag{10}$$

All considered bands are symmetric except the 4.3 μm band of CO_2 that has an upper limit. For the asymmetric band the non-defined band limit is calculated from the following equation:

$$\nu_{u,k} - \nu_{l,k} = \frac{A_k}{1-\tau_k} = \Delta\nu_k \tag{11}$$

Finally, the Beer's law is applied to calculate the absorption coefficient for the band k via the following equation:

$$\kappa_k = -\frac{1}{L}\ln(\tau_k) \tag{12}$$

For the spectral "clear" windows that are in between the limits of the absorption bands, the absorption coefficient is set equal to zero. To make sure that the entire wavelength spectrum is covered by the bands, $\lambda_{min} = 0$ and $\lambda_{max} T_{min} = 50{,}000$ are proposed [3]. Here λ_{min} and λ_{max} are the minimum and the maximum wavelength limits of the wavelength spectrum and T_{min} is the minimum expected gas temperature in the domain, which is taken equal to 1000 K in the calculated furnace. The computed band limits are given in Table 1.

The mean beam length L, which is required for the calculation of the absorption coefficient, is determined based on the average cell volume in the calculation domain. $L = 4.7$ cm is used in this work. Another alternative is to use the mean beam length for the whole enclosure [7], which is the furnace. The first approach has the disadvantage that the final outcome is somewhat dependent on the grid resolution, but it is consistent with the EWBM variant, which is applied here and has been developed for isothermal gas radiation. The latter condition is only fulfilled in a cell volume but cannot be assumed for the entire furnace domain.

Table 1
Division of the wavelength spectrum into four gas absorption bands and five gas clear windows

Band	Lower limit (μm)	Upper limit (μm)	Absorption coefficient (m^{-1})
1	0	2.54	0
2	2.54	2.75	EWBM
3	2.75	4.15	0
4	4.15	4.47	EWBM
5	4.47	5.31	0
6	5.31	7.60	EWBM
7	7.60	12.55	0
8	12.55	18.68	EWBM
9	18.68	50	0

3. Overview of the furnace/reactor calculations

3.1. Reactor model

In the plug flow reactor model, a set of mass balances for the process gas species is solved simultaneously with the energy and the pressure drop equation. The steady-state mass balance for a component j in the process gas mixture over an infinitesimal volume element with cross-sectional surface area Ω, circumference ω, and length dz is given by

$$\frac{dF_j}{dz} = \left(\sum_{k=1}^{n_R} n_{kj} r_k\right)\Omega \tag{13}$$

The energy equation is given by

$$\sum_j F_j c_{pj} \frac{dT}{dz} = \omega q + \Omega \sum_k r_k(-\Delta H_k) \tag{14}$$

The pressure drop equation, accounting for friction and changes in momentum, is given by

$$\frac{dp}{dz} = \alpha\left(\frac{2f}{d_t} + \frac{\zeta}{\pi r_b}\right)\rho_g u^2 + \alpha\rho_g u\frac{du}{dz} \tag{15}$$

The process gas temperature profile, conversion, and product concentration profiles can be calculated based on an imposed heat flux profile or an imposed external tube skin temperature profile. In this work, calculations are performed using a heat flux profile obtained from a CFD furnace calculation. The reactor model that is described above is coupled to a detailed reaction network for the steam cracking of hydrocarbons, containing over 1000 reactions among 128 species. A detailed description of the reactor model and the reaction mechanism for the steam cracking of hydrocarbons can be found in Van Geem et al. [8] and Heynderickx and Froment [9].

3.2. Furnace model

3.2.1. Flow

The calculation of the steady-state flue gas flow pattern and temperature profile in the furnace is based on the Reynolds-averaged Navier Stokes equations. The continuity, momentum and energy conservation equations are given by

$$\nabla\cdot(\rho\vec{v}) = 0 \tag{16}$$

$$\nabla\cdot(\rho\vec{v}\vec{v}) = -\nabla p + \nabla\cdot(\bar{\bar{\tau}}) + \rho\vec{g} \tag{17}$$

$$\nabla\cdot(\vec{v}(\rho E + p)) = \nabla\cdot\left(k_{eff}\nabla T - \sum_j h_j\vec{J}_j + (\bar{\bar{\tau}}_{eff}\cdot\vec{v})\right) + q_{rad} \tag{18}$$

The discrete ordinates (DO) radiation model using the finite-volume (FV) formulation is used to determine the radiative heat flux contribution q_{rad} to the energy equation, as will be explained in detail later. The standard k–ε model [10] is used for

the calculation of the turbulent properties:

$$\nabla \cdot (\rho \vec{v} k) = \nabla \cdot \left(\left(\mu + \frac{\mu_t}{\sigma_k} \right) \nabla k \right) + G_k + G_b - \rho\varepsilon \quad (19)$$

$$\nabla \cdot (\rho \vec{v} \varepsilon) = \nabla \cdot \left(\left(\mu + \frac{\mu_t}{\sigma_\varepsilon} \right) \nabla \varepsilon \right) + C_{1\varepsilon} \frac{\varepsilon}{k} (G_k + C_{3\varepsilon} G_b) - C_{2\varepsilon} \rho \frac{\varepsilon^2}{k} \quad (20)$$

Due to the high degree of turbulent mixing between fuel and oxidizer in the burner cups in the side-walls of the furnace (Fig. 2), complete combustion of the fuel gas in the cups is a reasonable assumption. This entails that only hot combustion products (hot flue gas) enter the radiation section of the furnace that is simulated in this work. The product species concentrations thus remain invariant in the simulated furnace domain. As a result, no explicit combustion calculations are to be performed in the context of the overall CFD modeling approach. If the furnace is heated with long flame burners, the furnace model has to be extended with mass balances for the fuel gas species and with a combustion model [11].

3.2.2. Radiation

As mentioned, to simulate the thermal radiation exchange under non-grey gas conditions the conservative variant of the discrete ordinates (DO) radiation model, called the finite-volume (FV) scheme and implemented in the FLUENT software package, is used [12–14]. The DO–FV method can be considered as a higher-order flux method and spans the entire range of optical thicknesses unlike the six-flux methods that are sufficiently accurate for optically thick media [15]. The DO–FV method considers the RTE in the direction $\vec{s}$ as a field equation:

$$\nabla \cdot (I(\vec{r}, \vec{s})\vec{s}) + (\kappa + \sigma_s) I(\vec{r}, \vec{s}) = \kappa n^2 \frac{\sigma T^4}{\pi} + \frac{\sigma_s}{4\pi} \int_0^{4\pi} I(\vec{r}, \vec{s}') \Phi(\vec{s} \cdot \vec{s}') \, d\Omega' \quad (21)$$

When modeling under non-grey gas conditions the above equation is solved band-wise. For the spectral intensity $I_\lambda(\vec{r}, \vec{s})$ Eq. (21) turns into

$$\nabla \cdot (I_\lambda(\vec{r}, \vec{s})\vec{s}) + (\kappa_\lambda + \sigma_s) I_\lambda(\vec{r}, \vec{s}) = \kappa_\lambda n^2 I_{b\lambda} + \frac{\sigma_s}{4\pi} \int_0^{4\pi} I_\lambda(\vec{r}, \vec{s}') \Phi(\vec{s} \cdot \vec{s}') \, d\Omega' \quad (22)$$

In Eq. (22), κ_λ is the spectral absorption coefficient, and $I_{b\lambda}$ is the black body intensity determined by the Planck function (Eq. (23)). The scattering coefficient σ_s, the scattering phase function Φ, and the refractive index n are assumed to be wavelength independent. The non-grey gas implementation divides the radiation spectrum into N wavelength intervals. The RTE (Eq. (22)) is integrated over each of these wavelength intervals $\Delta\lambda$, resulting in transport equations for the quantity $I_\lambda \Delta\lambda$. The behavior of the gas in each absorption band is assumed to be grey. The black body emission in the wavelength band per unit solid angle is

$$I_{b\lambda} = (f(n\lambda_u T) - f(n\lambda_l T)) n^2 \frac{\sigma T^4}{\pi} \quad (23)$$

where λ_u and λ_l are the upper and the lower wavelength band limits, respectively and $f(n\lambda T)$ is the fractional black body function. Finally, the total radiation intensity in each direction $\vec{s}$ and position $\vec{r}$ is calculated using the following equation:

$$I(\vec{r}, \vec{s}) = \sum_\kappa I_{\lambda_\kappa}(\vec{r}, \vec{s}) \Delta\lambda_\kappa \quad (24)$$

The summation is performed over all wavelength bands.

The boundary conditions in case of non-grey/DO–FV modeling are applied on a band basis. The radiative flux in a band leaving a surface is

$$q_{out,\lambda} = (1 - \varepsilon_{w,\lambda}) q_{in,\lambda} + \varepsilon_{w,\lambda} (f(n\lambda_u T) - f(n\lambda_l T)) n^2 \sigma T_w^4 \quad (25)$$

where $\varepsilon_{w,\lambda}$ is the wall emissivity in the band. $q_{in,\lambda}$ is the incident radiative heat flux on the surface, within the wavelength band interval $\Delta\lambda$, calculated from

$$q_{in,\lambda} = \Delta\lambda \int_{\vec{s}\cdot\vec{n}>0} I_{in,\lambda} \vec{s} \cdot \vec{n} \, d\Omega \quad (26)$$

3.3. Coupled furnace/reactor simulations

In order to evaluate the effect of high-emissivity wall coatings on the furnace thermal efficiency, coupled furnace (fire-side)–reactor (process-side) calculations are performed. A schematic diagram of the complete simulation procedure is shown in Fig. 1. In the CFD furnace calculations the set of partial differential equations along with the boundary and inlet conditions is solved with the finite-volume method using a segregated solver and the SIMPLE algorithm for pressure–velocity coupling. As explained above the DO–FV method is used for non-grey gas radiation modeling. The local band absorption coefficients are calculated by means of the EWBM that has been implemented in a user-defined function. The latter is plugged

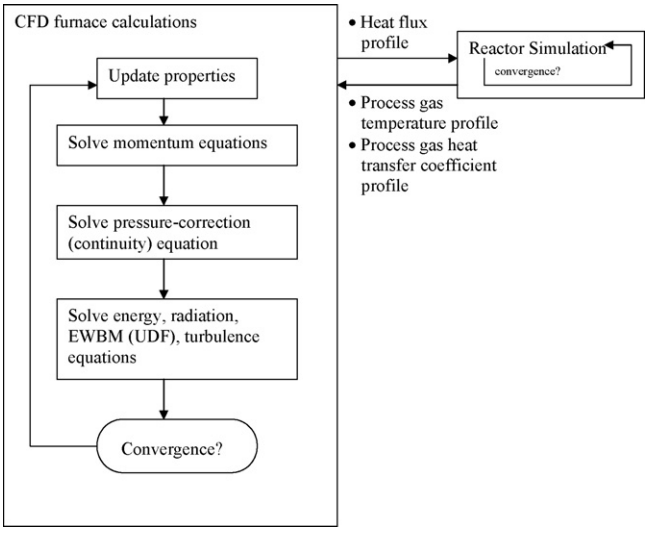

Fig. 1. Overview of the coupled furnace/reactor calculations.

into the CFD solver. The sequence of steps in the CFD furnace calculations (Fig. 1) is repeated several times until a converged solution is found for all calculated variable fields. The CFD furnace simulation provides the heat flux profile along the reactor length, which is the input for the reactor simulation software. Next, the reactor simulation updates the process gas temperature profile and the process gas heat transfer coefficient profile. Those two profiles are set as boundary conditions for the CFD furnace calculations. This two-way coupling is repeated several times until convergence of both the furnace and the reactor simulation is obtained.

4. Furnace geometry and operating conditions

The main design specifications and operating conditions of the simulated industrial naphtha cracking furnace are summarized in Tables 2 and 3, respectively. The side and the top view of the simulated furnace are given in Figs. 2 and 3, respectively. Due to the symmetry consideration only half of the furnace and the reactors needs to be simulated. Eight reactor coils with seven passes each, are suspended in two staggered rows in the furnace. The composition of naphtha that is cracked in these coils is summarized in Table 3: a feed of 9 paraffins, 20 isoparaffins, 23 naphthenes and 10 aromatics is considered. The furnace is heated by means of 224 radiation burners positioned in 16 rows of burners in the front wall (A wall) and 16 rows of burners in the rear wall (C wall). As mentioned in Section 3.2.1, complete fuel combustion in the burner cups is assumed and only hot combustion products (hot flue gas) enter the radiation section of the furnace. The flue gas species concentrations (Table 3) remain invariant in the simulated domain. Six hundred and fifty-three thousand and eight hundred and thirty-six (653,836) cells are used to discretize the physical domain between the furnace walls, the symmetry plane and the reactor tubes.

Table 2
Furnace specifications

Furnace	
Height, z (m)	7.32
Length, y (m)	11.83
Width, x (m)	1.7
Thickness of refractory (m)	0.23
Thickness of insulation (m)	0.05
Thickness of casing (m)	0.005
Reactor coils	
Number of reactors	8
Reactor length (m)	56.6684
External tube diameter (m)	0.1319
Internal tube diameter (m)	0.1143
Burners	
Number of radiation burners	224
Diameter of burner nozzle (m)	0.065
Diameter of burner plate (m)	0.356
Material properties	
Emissivity of furnace wall	Table 4
Emissivity of tube skin	0.85
Thermal conductivity of refractory wall (W/(m K))	0.394
Thermal conductivity of insulation (W/(m K))	0.19
Thermal conductivity of casing (W/(m K))	56
Thermal conductivity of tube skin (W/(m K))	26.05

Table 3
Furnace and reactor operating conditions

Firing conditions	
Flue gas flow rate (total) (kg/s)	1.23242
Flue gas composition (wt%)	
CO_2	0.1220
H_2O	0.1180
O_2	0.0366
N_2	0.7234
Flue gas inlet temperature (K)	1871.84
Reactor operating conditions	
Feedstock	Naphtha
Feedstock composition (wt%)	
Paraffins (9 components)	34.70
Iso-paraffins (20 components)	38.29
Naphthenes (23 components)	19.68
Aromatics (10 components)	7.33
Feedstock feed rate (kg/s) (1 coil)	0.729
Steam dilution (kg_{steam}/kg_{feed})	0.4
Coil inlet temperature (K)	873
Coil inlet pressure (atm)	2.532

5. Results and discussion

The goal of this work is to investigate whether the furnace wall emission coefficient influences the heat fluxes to the reactor tubes and the thermal efficiency of the entire furnace. The heat fluxes determine the process gas temperature inside the coils and consequently the naphtha conversion and olefin yields. An improvement in thermal efficiency of the furnace by using high-emissivity wall coatings can be translated into an increase in the yields or a decrease in the required fuel input. Two coupled furnace/reactor simulations are performed. The two simulations

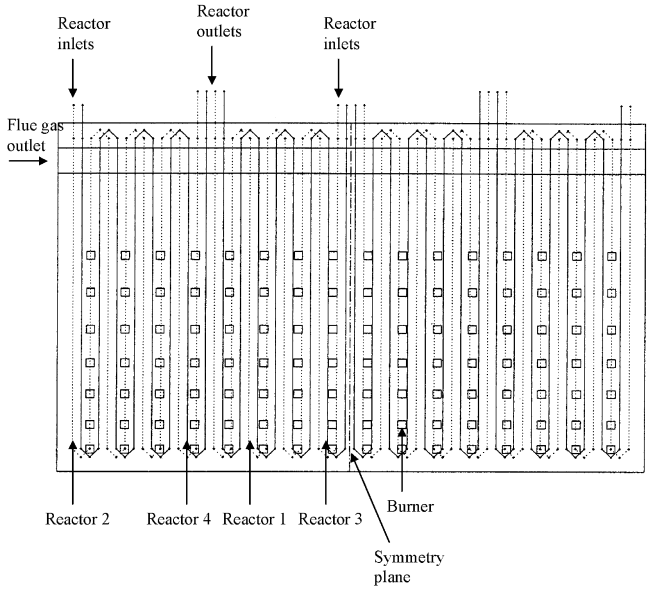

Fig. 2. Front view of the industrial steam cracking furnace.

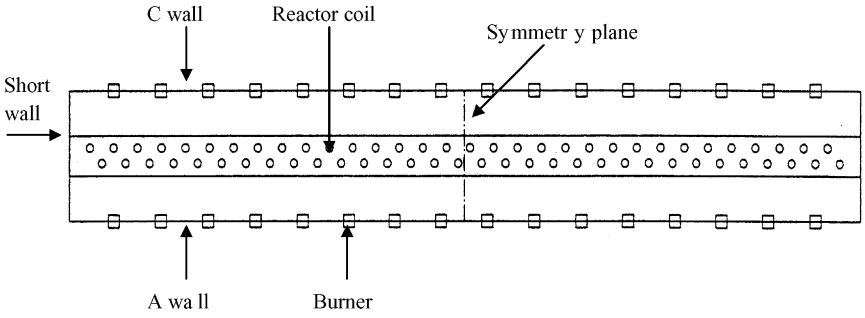

Fig. 3. Top view of the industrial steam cracking furnace.

differ only with respect to the furnace wall emissivity value. Contrary to the gas, opaque, grey-diffuse furnace wall and tube skin surfaces are assumed in both cases. The index of refraction is set equal to 1 and scattering is neglected. In the first simulation (case 1) the furnace wall emissivity is low: $\varepsilon_w = 0.386$. In the second simulation (case 2) the wall is coated and an increased furnace wall emissivity value is used in the calculations: $\varepsilon_w = 0.738$. The grey wall emissivities are calculated from non-grey values according to [16]:

$$\sum_{z=1}^{17} \varepsilon_{w,z} \cdot \mathrm{sum}\Delta\lambda_z = \varepsilon_{w,\mathrm{grey}} \tag{27}$$

$$\sum_{z=1}^{17} \mathrm{sum}\Delta\lambda_z = 1 \tag{28}$$

The emissivity values $\varepsilon_{w,z}$ of the solid wall material for 17 different wavelength bands, considered in this work, are given in Table 4 [16,17]. $\mathrm{sum}\Delta\lambda_z$ is the fraction of the black body emissive power for the band z over an interval $\Delta\lambda$.

The simulations show an average increase in the total heat flux to the reactor tubes of 2.1% when the furnace wall emissivity changes from 0.386 to 0.738. This results in an overall rise in thermal efficiency from 40.0% to 40.9%. In order to fully understand the origin of this difference, the surface incident and outgoing radiation fluxes per band for both the furnace wall and the reactor tubes are evaluated. In Fig. 4, the averaged net incident radiation flux on reactor 1 in each band is compared for both cases. The net surface incident radiation flux is defined by

$$q_{\mathrm{net,in},\lambda} = q_{\mathrm{in},\lambda} - q_{\mathrm{out},\lambda} = \varepsilon_{w\lambda} q_{\mathrm{in},\lambda} - \varepsilon_{w\lambda}(f(n\lambda_u T) - f(n\lambda_l T)) n^2 \sigma T_w^4 \tag{29}$$

In Fig. 4, the numbers on the horizontal axis correspond to the band numbers as used in Table 1. Band nos. 1, 3, 5, 7 and 9 are clear windows; the flue gas in these bands is non-absorbing and non-emitting. Band nos. 2, 4, 6 and 8 are absorption bands in which the flue gas does absorb and emit radiation. It can readily be seen that the averaged net incident radiation flux on reactor 1 is positive in all bands. However, when comparing the simulation results between case 1 ($\varepsilon_w = 0.386$) and case 2 ($\varepsilon_w = 0.738$) a different trend in the change of the averaged net incident radiation flux on the reactor is observed. When the wall emission coefficient rises from 0.386 to 0.738, the averaged net incident radiation flux on reactor 1 increases in the clear bands and decreases in the absorption bands. The outcome of these two reverse effects is a total increase in the averaged net incident radiation flux on reactor 1 by 2198 W/m^2 or 2.28%. A comparable result is found for the other reactors. This increase in the averaged net incident radiation on the reactor coils results in an increase in the furnace thermal efficiency. As no changes have been made to the boundary conditions applied to both simulation cases, the observations described above should be attributed to the difference in furnace wall emissivity between the two simulation cases.

Fig. 5 shows the averaged net surface outgoing radiation flux for all furnace walls for each band. The latter is defined by

$$q_{\mathrm{net,out},\lambda} = q_{\mathrm{out},\lambda} - q_{\mathrm{in},\lambda} = \varepsilon_{w\lambda}(f(n\lambda_u T) - f(n\lambda_l T)) n^2 \sigma T_w^4 - \varepsilon_{w\lambda} q_{\mathrm{in},\lambda} \tag{30}$$

In the clear windows, there is a positive averaged net furnace wall outgoing radiation flux, whereas in the absorption bands there is a negative averaged net furnace wall outgoing radiation flux (this corresponds to a positive averaged net furnace wall incident radiation flux). Furthermore, the change in the furnace wall emission coefficient from $\varepsilon_w = 0.386$ to 0.738 decreases the negative averaged net furnace wall outgoing radiation flux (or increases the positive averaged net furnace wall incident

Table 4
Solid wall emissivity values for 17 wavelength bands [17]

Band	Division (μm)	Furnace wall[a]	Coating[a]
1	18<	0.85	0.95
2	12.0–18.0	0.85	0.95
3	10.6–12.0	0.85	0.95
4	10.2–10.6	0.85	0.95
5	9.6–10.2	0.85	0.95
6	9.2–9.6	0.85	0.95
7	9.0–9.2	0.85	0.95
8	5.0–9.0	0.8	0.92
9	4.8–5.0	0.5	0.85
10	4.0–4.8	0.36	0.77
11	2.9–4.0	0.3	0.68
12	2.3–2.9	0.2	0.65
13	2.0–2.3	0.13	0.62
14	1.7–2.0	0.13	0.62
15	1.5–1.7	0.15	0.62
16	1.2–1.5	0.15	0.62
17	<1.2	0.13	0.62

[a] Grey wall emissivity ($\varepsilon_{w,\mathrm{grey}}$): furnace wall: 0.386; coating: 0.738.

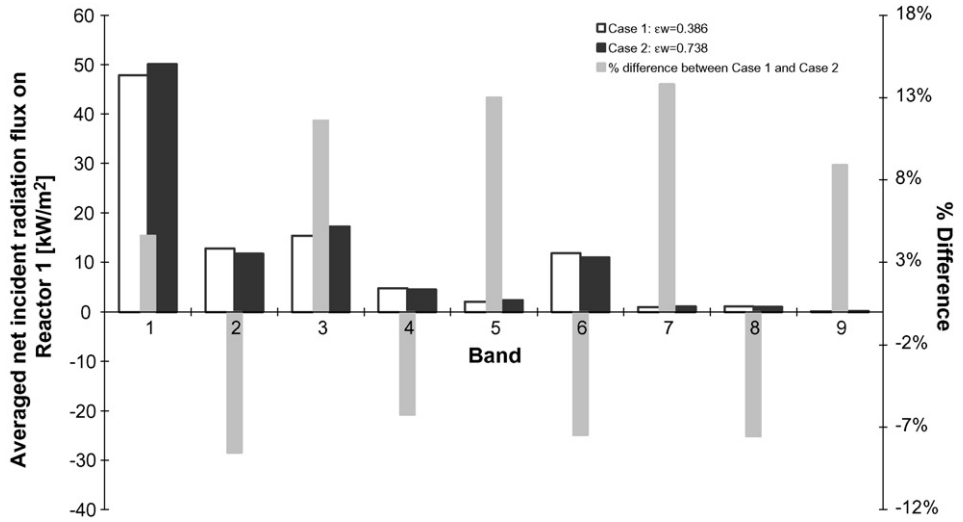

Fig. 4. Averaged net incident radiation flux on Reactor 1 (Fig. 2) in each band for both simulation cases and percent difference in the net reactor surface incident radiation between the two cases. Band nos. 1, 3, 5, 7 and 9 are clear bands. Band nos. 2, 4, 6 and 8 are absorption bands.

radiation flux) in the absorption bands and increases the positive averaged net furnace wall outgoing radiation flux in the clear windows. Thus, when increasing the furnace wall emissivity, the reactor tubes receive more radiation energy in the clear windows and less radiation energy in the absorption bands (Fig. 4).

Fig. 6 explains the furnace wall effects. The averaged blackbody emission flux from all furnace walls and the averaged furnace wall incident radiation flux $q_{\mathrm{in},\lambda}$ (see Eq. (26)) for all bands in case 1 are presented. In all clear windows, the averaged blackbody emission flux is higher than the averaged furnace wall incident radiation flux. This is expected because the incident radiation on the furnace wall in a clear window is determined by the radiation energy emitted by the furnace wall itself, by the reactor tubes, which are at lower temperature, and by the heat loss at the furnace outlet through the clear window. More specifically, since part of the radiation energy emanating from a furnace wall surface in a clear window is absorbed by the reactor coils or is lost at the outlet (no absorption/emission by the gas takes place in the flue gas clear windows), it is physically impossible that the averaged furnace wall incident radiation is higher than the averaged blackbody emission from the furnace walls, which is the maximum possible amount of the averaged emitted energy from the furnace walls. On the other hand, the reverse phenomenon is seen in the absorption bands. The averaged furnace wall blackbody emission is lower than the averaged furnace wall incident radiation. This is a consequence of the presence of the absorbing and emitting gas in the furnace domain. The flue gas, being at higher temperature than the furnace wall, emits additional (as compared to the clear windows) radiation energy towards the furnace wall, which results in a higher averaged furnace wall incident radiation as compared to the averaged furnace wall blackbody emission. Finally, as the averaged blackbody emission in a band $((f(n\lambda_{\mathrm{u}}T) - f(n\lambda_{\mathrm{l}}T))n^2\sigma T_{\mathrm{w}}^4)$ is higher

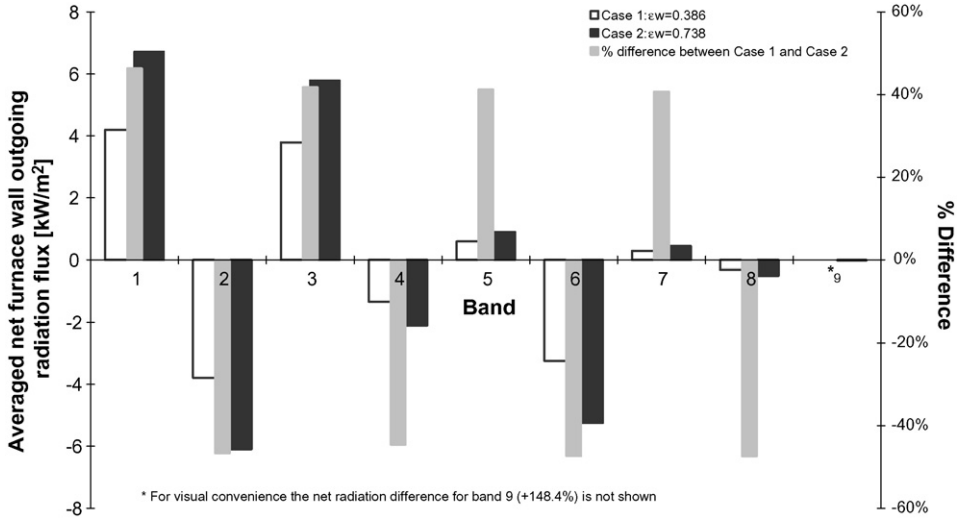

Fig. 5. Averaged net furnace wall outgoing radiation flux in each band for both simulation cases and percent difference in the net furnace wall outgoing radiation between the two cases. Band nos. 1, 3, 5, 7 and 9 are clear windows. Band nos. 2, 4, 6 and 8 are absorption bands.

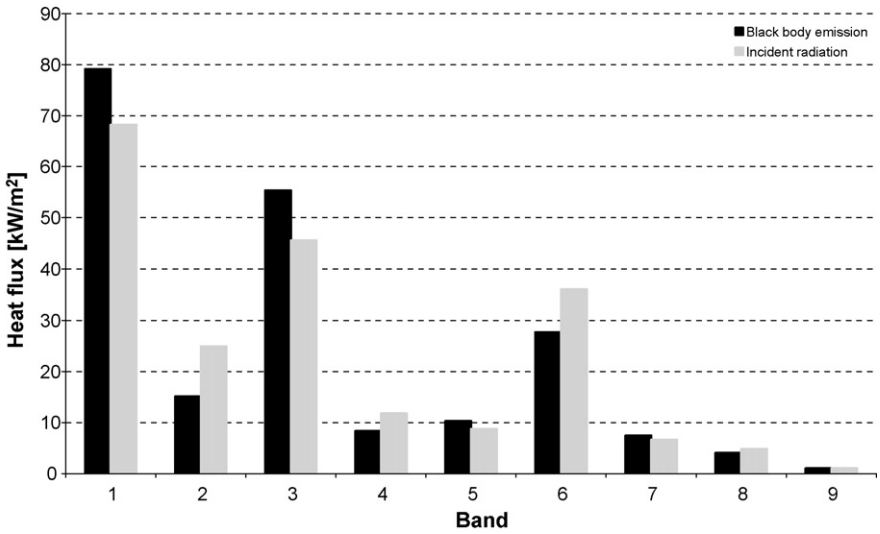

Fig. 6. Comparison between the averaged furnace wall black body emission flux and the averaged furnace wall incident radiation flux in each band. Band nos. 1, 3, 5, 7 and 9 are clear windows. Band nos. 2, 4, 6 and 8 are absorption bands.

than the averaged furnace wall incident radiation ($q_{in,\lambda}$) in the clear windows on the one hand and vice versa in the absorption bands on the other hand, it must be concluded that the averaged net furnace wall outgoing radiation will be positive in the clear windows and negative in the absorption bands (see Eq. (30) and Fig. 5). Furthermore, an increase in the furnace wall emissivity value multiplying the two terms on the right hand side of Eq. (30) will result in an increase in the averaged net furnace wall outgoing radiation in the clear bands and a decrease in the averaged net furnace wall outgoing radiation in the absorption bands. Both effects are shown in Fig. 5.

So far, the effects of the furnace wall coating on the net incident and net outgoing band radiation fluxes at the furnace wall and tube surfaces have been discussed in Figs. 4–6. Figs. 7 and 8 provide the "link" between the "furnace wall-effect" and the "tube skin-effect". In Fig. 7, typical horizontal profiles of the sum of incident radiation fluxes in the clear windows along the furnace width for the cases 1 and 2 are presented. The profiles are taken at a height of 3.775 m and a length of 1.732 m. They start from the furnace A wall in-between two burners and end up on the opposite C wall. The corresponding profiles for the sum of incident radiation fluxes in the absorption bands are presented in Fig. 8. It can be seen that a rise in the wall emission coefficient results in an increase in the incident radiation flux travelling through the flue gas in the clear bands (Fig. 7) and a decrease in the incident radiation flux travelling through the flue gas in the absorption bands (Fig. 8) all the way from the walls to the tubes. This corresponds with the results shown in Fig. 4: an increase in the averaged net incident radiation flux on the reactor coils in the clear windows and a decrease in the averaged net incident radiation flux on the reactor coils in the absorption bands when increasing the furnace wall emissivity. The pro-

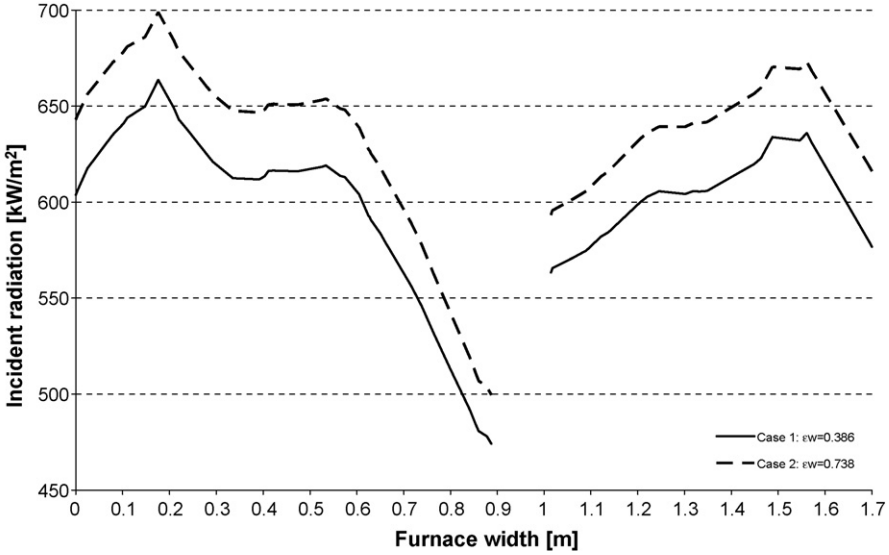

Fig. 7. Horizontal profile of the sum of incident radiation fluxes in the clear bands along the width of the furnace between the A and C walls (see Fig. 3). Height = 3.775 m and length = 1.732 m.

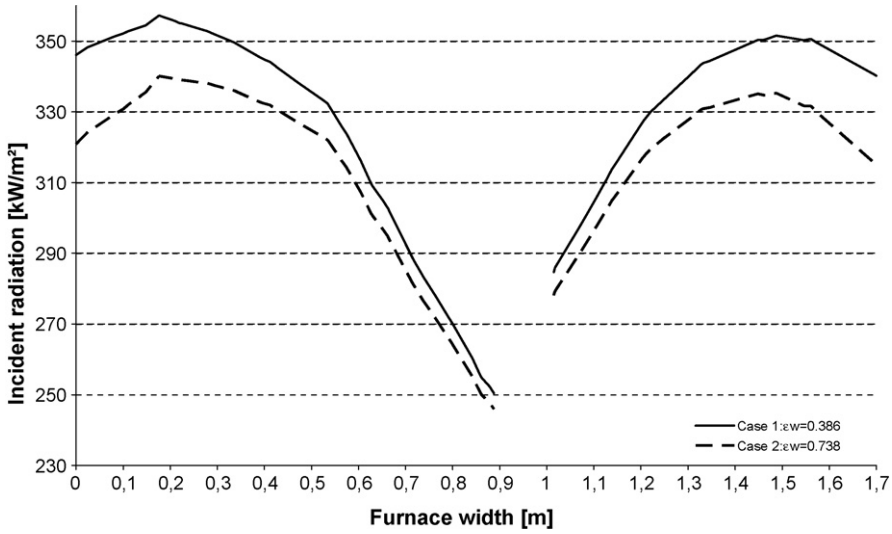

Fig. 8. Horizontal profile of the sum of incident radiation fluxes in the absorption bands along the width of the furnace between the A and C walls (see Fig. 3). Height = 3.775 m and length = 1.732 m.

files in Figs. 7 and 8 also correspond with the profiles presented in Fig. 5. More specifically, the increase in incident radiation flux travelling through the flue gas in the clear windows when increasing the wall emissivity (Fig. 7) is linked to the increase in the averaged net furnace wall outgoing radiation flux in the clear windows when increasing the wall emissivity (Fig. 5). In the same way, the decrease in incident radiation flux travelling through the flue gas in the absorption bands when increasing the wall emissivity (Fig. 8) is linked to the decrease in the averaged net furnace wall outgoing radiation flux in the absorption bands when increasing the wall emissivity (Fig. 5). Finally, it is noted that the gradual decrease in the incident radiation fluxes as the centre of the furnace is approached (Figs. 7 and 8) is due to the "heat sink" in the centre of the furnace, where the reactor tubes are suspended.

Overall, it is concluded that the physical mechanism that determines the increase in thermal efficiency is the reallocation of radiation energy among clear windows and absorption bands on the furnace walls. Radiation energy originating from the flue gas (radiated from the absorption bands) is partially converted, due to wall absorption and re-emission, into furnace wall outgoing radiation in the clear windows. A higher furnace wall emission coefficient will enhance this flue gas radiation energy reallocation effect on the furnace walls by increasing the furnace wall outgoing radiation in the clear windows and decreasing the furnace wall outgoing radiation in the absorption bands. Since radiation travelling through the flue gas in the clear windows can reach the reactor tubes without partially being absorbed by the flue gas the overall heat flux towards the reactor tubes increases.

The increase in furnace thermal efficiency when increasing the furnace wall emissivity has an influence on the naphtha conversion and the product yields. Fig. 9 shows typical process gas temperature, naphtha conversion and product yield profiles along the tube length of Reactor 4. A comparison of the most important simulation results between case 1 and case 2 for Reactor 4 is presented in Table 5. The furnace thermal efficiency rises from 40.0% to 40.9% by applying a high-emissivity coating on

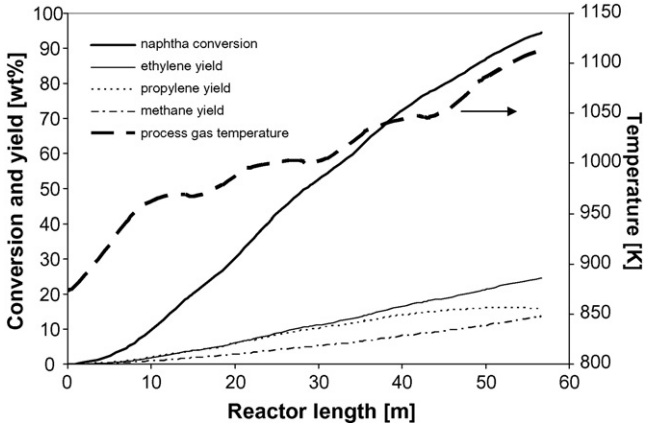

Fig. 9. Typical simulation results for the most important variable profiles along the length of reactor 4 (see Fig. 2). $\varepsilon_w = 0.738$, reactor operating conditions: Table 3.

the furnace wall (case 2). As a result, the naphtha conversion rises from 93.4 wt% to 94.5 wt% and the ethylene yield rises from 24.1 wt% to 24.6 wt%. Similar results are calculated for the other reactors (not shown). These differences are small but, considering the industrial importance and scale of the steam cracking process, significant.

Table 5
Simulation results

	Case 1	Case 2
Furnace efficiency (%)	40.0	40.9
Reactor 4 (see Fig. 2)		
Max heat flux (kW/m^2)	136	139
Coil outlet temperature (K)	1104	1112
Max tube skin temperature (K)	1272	1279
Naphtha conversion (%)	93.4	94.5
Ethylene yield (%)	24.1	24.6
Propylene yield (%)	15.8	15.7
Max coking rate ($\times 10^{-6}$ kg/(m^2 s))	7.36	8.33

6. Conclusions

The application of high-emissivity coatings on the walls of a naphtha cracking furnace increases the thermal efficiency of the furnace and improves the cracking results. The increase in thermal efficiency should be attributed to the energy reallocation mechanism among clear windows and absorption bands that takes place on the furnace walls. Incident radiation on the furnace wall originating from flue gas absorption bands is partially converted due to wall absorption and re-emission into outgoing radiation from the furnace wall in the clear windows. Applying a high-emissivity coating on the furnace wall decreases the net outgoing radiation from the furnace wall in the absorption bands and increases the net outgoing radiation from the furnace wall in the clear windows. Since radiation that is emitted by the furnace wall and travels through the flue gas in the clear windows can reach the reactor tubes without partially being absorbed by the flue gas, contrary to radiation that is emitted by the furnace wall and travels through the flue gas in the absorption bands, the thermal efficiency of the furnace increases.

Acknowledgment

We would like to acknowledge the Fund for Scientific Research (FWO) for financial support through project no. G.0070.03.

References

[1] J.C. Hellander, Hydrocarbon Process. 76 (1997) 91–96.
[2] Y.U. Khan, D.A. Lawson, R.J. Tucker, J. Inst. Energy 71 (1998) 21–26.
[3] Fluent 6.2 User's Guide, Fluent Inc., Lebanon, NH, 2005.
[4] D.K. Edwards, Adv. Heat Transfer 12 (1976) 115–193.
[5] D.K. Edwards, A. Balakrishnan, Int. J. Heat Mass Transfer 16 (1973) 25–40.
[6] J. Ströhle, P.J. Coelho, Int. J. Heat Mass Transfer 45 (2002) 2129–2139.
[7] F. Liu, H.A. Becker, Y. Bindar, Int. J. Heat Mass Transfer 41 (1998) 3357–3371.
[8] K.M. Van Geem, G.J. Heynderickx, G.B. Marin, AIChE J. 50 (2004) 173–183.
[9] G.J. Heynderickx, G.F. Froment, Ind. Eng. Chem. Res. 35 (1996) 2183–2189.
[10] B.E. Launder, D.B. Spalding, Lectures in Mathematical Models of Turbulence, Academic Press, London, 1972.
[11] G.D. Stefanidis, B. Merci, G.J. Heynderickx, G.B. Marin, Comput. Chem. Eng. 4 (2006) 635–649.
[12] G.D. Raithby, E.H. Chui, J. Heat Transfer 112 (1990) 415–423.
[13] S.W. Baek, K.Y. Kim, J.S. Kim, Numer. Heat Transfer B 34 (1998) 419–437.
[14] G.D. Raithby, Numer. Heat Transfer B 35 (1999) 389–405.
[15] E.D. Keramida, H.H. Liakos, M.A. Founti, A.G. Boudouvis, N.C. Markatos, Int. J. Heat Mass Transfer 43 (2000) 1801–1809.
[16] G.J. Heynderickx, M. Nozawa, AIChE J. 51 (2005) 2721–2736.
[17] J.D. Jackson, C.C. Yen, Ceramics in Energy Applications Conference, Pergamon Press, London, 1994, pp. 159–174.